Metals & corrosion

Effect of pull-down rate and power on electromagnetic separation of hypereutectic Ti–Si alloy under vacuum

Ruifeng Zhang[1,2], Junpeng Wang[1,2], Kuisong Zhu[3], Yun Lei[1,2], Wenhui Ma[1,2], and Guoqiang Lv[1,2,*]

[1] *Faculty of Metallurgical and Energy Engineering, Kunming University of Science and Technology, Kunming 650093, China*
[2] *State Key Laboratory of Complex Nonferrous Metal Resources Cleaning Utilization in Yunnan Province, Kunming 650093, China*
[3] *School of Vanadium and Titanium, Panzhihua University, Panzhihua 617000, China*

ABSTRACT

In the present study, numerical and experimental methods were used to investigate the effects of the process parameters on the enrichment of primary Si by separation of hypereutectic Ti-89 wt.% Si alloy melts during directional solidification. The results indicated that the separation of the primary Si from Ti-89 wt% Si alloy melts significantly depends on the pull-down rate of the melts, and the flow velocity of the melts decreases as the pull-down rate increases, which reduces the separation and enrichment effects of the primary Si during the electromagnetic directional solidification process. Conversely, with the increase in power, the convection and heat transfer of the melt are enhanced, which promotes the separation and enrichment of primary Si. Furthermore, the enrichment of silicon was analyzed by ICP (Inductive coupled plasma emission spectrometer), and it was found that with the power increasing from 3.8 to 5.4 kW, the content of Ti in the silicon enrichment layer decreased from 4.16 to 2.08%.

Introduction

V–Ti magnetite of Panzhihua is complex iron ore with coexisting elements of vanadium and titanium. It accounts for more than 90% of China's titanium reserves [1]. With the continuous utilization of vanadium–titanium magnetite concentrate in Panzhihua area, a large number of high-titanium blast furnace slags have accumulated [2, 3]. Due to the lack of application, a large amount of slag would occupy space and pollute the environment, which also wastes Ti resources. Therefore, the healthy development and comprehensive utilization of titanium resources are very significant. In recent years, efficiency, low-cost, and eco-friendly methods for recovering titanium from high-titanium blast furnace slag have been widely studied, such as blast furnace

Handling Editor: P. Nash.

Address correspondence to E-mail: lvguoqiang_ok@aliyun.com

🖄 Springer

slag modification-selective enrichment of titanium-containing minerals [4, 5], high-temperature carbonization–low-temperature chlorination process [6], hydrometallurgy [7, 8], preparation of alloys from high-titanium slag [9]. However, the titanium recovery rate of blast furnace slag modification-selective enrichment of titanium-containing minerals process is low and the cost is high. The high-temperature carbonization–low-temperature chlorination process has the problems of difficult treatment of chlorination residue and high power consumption. Hydrometallurgy needs to solve the potential secondary pollution problems such as waste acid and waste alkali in the production process. High-titanium blast furnace slag can successfully prepare Ti–Si alloy through metal thermal reduction, which is often used as a deoxidizer or alloying agent for converter steelmaking. And these methods only stay at the laboratory level or are difficult to consume a large number of high-titanium blast furnace slag and unable to industrialize, so it is necessary to find a new way to efficiently utilize high silicon Ti–Si alloy. Zhu et al. successfully separated primary Si and Ti–Si alloys from high silicon titanium-silicon alloy melt by electromagnetic directional solidification [10]. Primary Si after further refining and purification may be used as raw material for the production of solar-grade multicrystalline silicon. Ti–Si eutectic alloy has been widely studied due to its excellent casting properties such as low melting point and good fluidity.

During the process of electromagnetic directional solidification, the melt is driven to flow by the effect of electromagnetic stirring (EMS), which strongly influences grain growth and temperature distribution. EMS force inside the melt can influence the characteristics of the flow and the shape of the alloy melt. Meantime, the flow would enhance the process of the heat transfer and the mass transfer of the melt, which would disturb the continuity of the crystal growth. It is significant to study the flow and heat transfer inside the melt. However, electromagnetic directional solidification is an invisible process of high temperature and high vacuum. It is difficult to measure the flow pattern and heat transfer of the melt in practice. Therefore, numerical simulation has great potential for exploring the heat transfer characteristics and melt fluidity in the directional solidification process. The results lay a foundation for further exploring the mechanism of separating primary Si and Ti–Si Alloys by electromagnetic directional solidification. At present, many scholars have carried out numerical simulation analysis of the directional solidification process. Yu et al. studied the melt convection pattern in the process of directional solidification of crystalline silicon. It was found that under the action of a traveling magnetic field, the current parameters have a great influence on the Lorentz force, melt convection, and thermal field. By adjusting the electromagnetic parameters, the melt homogeneity can be improved and the quality of silicon ingot can be improved [11]. Chen et al. established a three-dimensional (3D), finite element model to study the flow field in the molten pool during electromagnetic directional solidification based on the experimental study. The numerical results show that the flow pattern of melt changes with the frequency from 10 to 100 kHz, and the electromagnetic stirring in the melt is more intense at low frequencies [12]. Yang et al. established a 3D finite element model using the commercial software ANSYS to study the effect of the horizontal flow of Ti–Al alloy melt on microstructure during directional solidification. As the power increases, the flow rate of the melt near the solid–liquid interface increases. And the experimental results also prove that the flow field in the melt can be regulated to obtain a situation conducive to the continuous growth of crystals by adjusting the heating power and current frequency [13]. Yang et al. enhanced the heat transfer of the traditional directional solidification process, which resulted in an improvement in crystal quality [14]. Yu et al. observed that the primary silicon would move up or down when a magnetic field is applied to the directional solidification separation process of an Al–Si alloy [15]. Lv et al. experimentally studied the flow and heat transfer behaviors during electromagnetic directional solidification and its influence on grain migration [16].

The main aim of this paper is to study the relations between the flow in the melt and the separation of the silicon phase. A physical model of flow and heat transfer in the electromagnetic directional solidification process was established. Based on that, the influence of the change in the pulling rate and the coil power on the flow field is studied. Further, the macro/microstructures of Ti–Si ingots by electromagnetic directional solidification were investigated.

Experimental procedure and numerical model

Experimental procedure

A hypereutectic Ti-89 wt% Si alloy was prepared from 62.3 g of pure Si and 7.7 g of Ti and then charged in a graphite crucible with an inner diameter of 30 mm and a length of 150 mm. The apparatus of an electromagnetically-induced furnace is shown in Fig. 1a. The experiment was carried out under the conditions of a vacuum of 10 Pa. The directional solidification distance was set to 5 cm. As shown in Fig. 1a, the raw composed of Ti sponges (99.5%) and pure Si (99.999 wt%) in the crucible was melted and kept at 1733 K for 20 min to homogenize its composition. The base and graphite crucible simultaneously moves down at set velocities. Due to intensive chilling from the cooling water in the base, the heat was removed from the bottom, a longitudinal temperature gradient was formed in the charge accordingly. In the directional solidification process, the temperature was measured at the melt surface of the center of the crucible at intervals of 5 min via a non-contact infrared thermometer, which was calibrated at the melting point of silicon with fluctuations of about

±15 °C. The directional solidification ingots were cut with a diamond wire cutter along its longitudinal cross-sectional center, and microstructure analysis was performed using an electron probe micro-analyzer (EPMA, JXA8230, JEOL, Japan). To study the relationship between the separation efficiency of Si and the electromagnetic stirring and vacuum directional solidification coupling external field strengthening, three samples were collected at the bottom of Si-rich layers and the silicon content was detected using ICP-AES.

Geometry definition

The commercial software COMSOL multiphysics was employed to calculate the flow fields inside Ti-89 wt% Si melt. Figure 1b gives the FE model and its grid generation. In the computational domain, the maximum size of the triangular mesh is set to 18.5 mm. Additionally, the quality of the mesh will significantly affect the accuracy of the calculation results, so it is necessary to refine the mesh in the melt area affected by the skin effect. Table 1 shows the physical parameters of the materials used in the calculation. Table 2 shows the thermo-physical and electromagnetic properties of the Ti-89 wt% Si (solid)
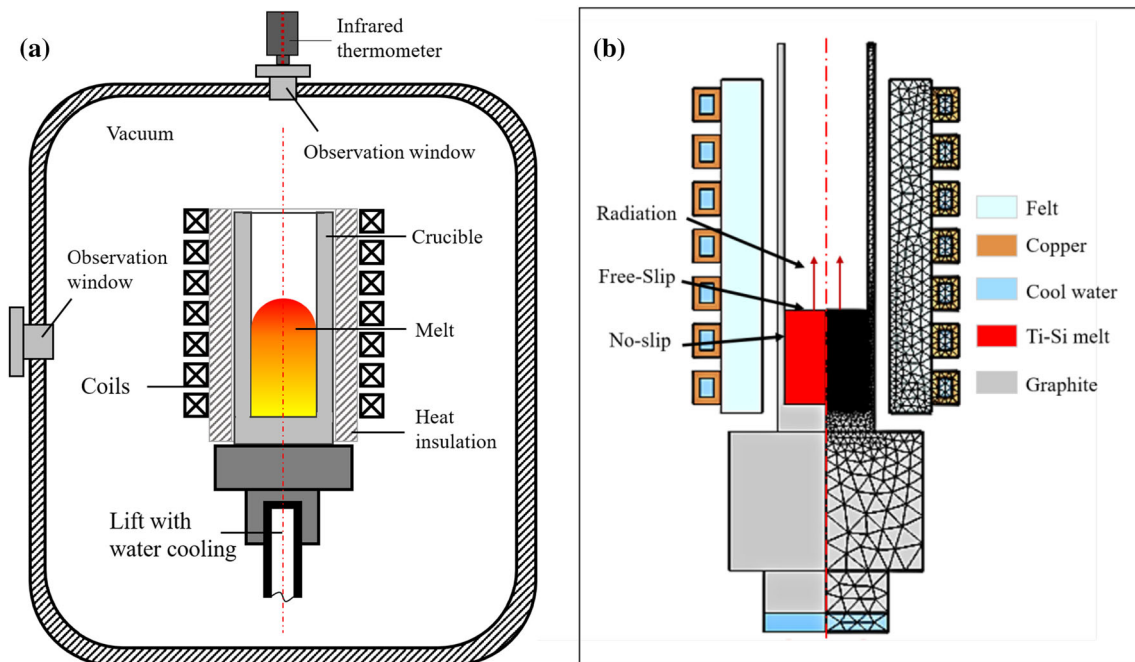
Figure 1 **a** Schematic diagram of vacuum directional solidification furnace; **b** 2D-axisymmetric FE model of the crucible with a charge and grid generation.

Table 1 Properties of materials used in the simulation

Properties	Coils	Crucible	Ti-89 wt% Si(Melt)	Insulator	Cool water
Electric conductivity (S m^{-1})	5.998×10^7	3×10^3	1.25×10^6	1	5.5×10^{-6}
Relative permeability	1	1	1	1	1
Density (kg m^{-3})	8940	1950	2577	520	1000
Dynamic viscosity (Pa s)	–	–	0.0012	–	–
Thermal conductivity (W (m K)$^{-1}$)	400	150·300/T	57.3	0.045	60
Specific heat capacity (J (kg K)$^{-1}$)	385	710	966.6	816	4182

and (melt) in the calculation. The physical parameters of the Ti-89 wt% Si alloy are calculated by JMAT Pro, and the rest of the parameters are from the material library that comes with the commercial software COMSOL multiphysics. It is assumed that the physical parameters of the Ti-89wt% Si after melting are independent of temperature.

Mathematical models

In this study, the directional solidification process involves a series of complex phenomena such as heat transfer, flow, and movement, which interact with each other. To save computing resources, some rationalization assumptions were made on the model as follows [17–20]:

1. A two-dimensional axisymmetric model was established for calculation, because the main component of the configuration is a cylindrical structure.
2. The influence of air convection in the furnace was ignored due to the lower pressure.
3. The melt is incompressible and treated as a homogeneous medium.
4. The radiating surfaces involved in the model are set as diffuse gray surface.
5. The latent heat of transformation of the Ti-89 wt% Si alloy phase system is regarded as the latent heat of transformation of single phase.

The magnetic field can be obtained by solving Maxwell's equations:

$$\nabla \times \boldsymbol{H} = \boldsymbol{J} \tag{1}$$

$$\boldsymbol{B} = \nabla \times \boldsymbol{A} \tag{2}$$

$$\boldsymbol{E} = -j\omega\boldsymbol{A} \tag{3}$$

$$\boldsymbol{J} = \sigma\boldsymbol{E} + j\omega\boldsymbol{D} \tag{4}$$

where $\boldsymbol{H}$ represents the magnetic field intensity (A m^{-1}), $\boldsymbol{J}$ represents the current density (A m^{-2}), $\boldsymbol{B}$ is the magnetic flux density (T), $\boldsymbol{E}$ is the electric field intensity (V m^{-1}), and $\boldsymbol{A}$ is the vector magnetic potential (AT), $\boldsymbol{D}$ is the electric displacement vector (C m^{-2}).

As a heat source in the heat transfers part of the model. It is given by

$$Q_e = Q_{rh} + Q_{ml} \tag{5}$$

The resistive losses and the magnetic losses are

$$Q_{rh} = 0.5 real(\boldsymbol{J} \cdot \boldsymbol{E}) \tag{6}$$

$$Q_{ml} = 0.5 real(i\omega\boldsymbol{B} \cdot \boldsymbol{H}) \tag{7}$$

During the directional solidification process, the thermal conduction between the charge and the crucible wall is described by the heat transfer equation as:

$$\rho C_p \cdot \nabla T = \nabla \cdot (k\nabla T) + Q_e \tag{8}$$

Table 2 Properties of the Ti-89 wt% Si(solid) and Ti-89 wt% Si(Melt) in the calculation

Properties	Ti-89 wt% Si(solid)	Ti-89 wt% Si(Melt)
Electric conductivity (S m^{-1})	500	1.25×10^6
Relative permeability	1	1
Thermal conductivity (W (m K)$^{-1}$)	45	57.3
Specific heat capacity (J (kg K)$^{-1}$)	995	966.6
Melting temperature (K)	1651	
Phase change enthalpy (J kg^{-1})	1.64×10^6	

where C_p, k and Q_e denote specific heat, thermal conductivity, and heating power per unit volume (heat source term), respectively.

For the radiation of the crucible in the furnace, the radiation equation is solved:

$$-\boldsymbol{n} \cdot (-k\nabla T) = \varepsilon(G - \sigma T^4) \tag{9}$$

$$G = G_m(J_a) + F_{amb}\sigma T_{amb}^4 \tag{10}$$

$$(1 - \varepsilon)G = J - \varepsilon\sigma T^4 \tag{11}$$

The furnace shell has circulating cooling water flowing through the whole process of the experiment, so the temperature of the furnace wall is set to a constant temperature. For the water-cooled heat exchange in the copper induction coil and the lifting platform, the convection heat exchange boundary is used, and the convection heat transfer coefficient is h determined by the following formula

$$\Pr = \frac{\mu C_P}{k'} \tag{12}$$

$$N_u = 0.023 Re^{0.8} Pr^{0.4} \tag{13}$$

$$\boldsymbol{h} = \varepsilon\frac{k'}{d}\boldsymbol{N_u} \tag{14}$$

$$-\boldsymbol{n} \cdot (-k'\nabla \boldsymbol{T}) = \boldsymbol{h} \cdot (\boldsymbol{T}_{\text{ext}} - \boldsymbol{T}) \tag{15}$$

where Pr is the Prandtl number, μ is the dynamic viscosity of the cooling water, C_P is the specific heat capacity of the cooling water, k' is the thermal conductivity (W/(m·K)), Re is the Reynolds number, N_u is the Nusselt number, ε is the correction coefficient, d is the pipe diameter, and $\boldsymbol{T}_{\text{ext}}$ is the cooling water temperature (K).

The melt flow by describing the fluid velocity and the pressure according to equations

$$\rho_l \nabla \cdot \boldsymbol{u} = 0 \tag{16}$$

$$\rho_l(\boldsymbol{u} \cdot \nabla)\boldsymbol{u} = \nabla \cdot \left[-pI + \mu\left(\nabla\boldsymbol{u} + (\nabla\boldsymbol{u})^T\right)\right] + \boldsymbol{F}_{\text{ext}} \tag{17}$$

where ρ_l is the density (kg m^{-3}), and μ is the viscosity (Pa·S). The source term $\boldsymbol{F}_{\text{ext}}$ is composed of gravity and electromagnetic force $\boldsymbol{F}_{\text{emf}}$ (N m^{-3}). $\boldsymbol{F}_{\text{emf}} = \boldsymbol{J} \times \boldsymbol{B}$, where $\boldsymbol{J},\boldsymbol{B}$ represent the current density in the melt and the magnetic field generated by the induction coil, respectively.

Liquid fraction B is introduced to describe the solid–liquid interface visually, and the equation is expressed [21]:

$$B = \begin{cases} 1 & T > T_m + \Delta T \\ \dfrac{(T - T_m + \Delta T)}{2\Delta T} & (T_m - \Delta T) \le T \le (T_m + \Delta T) \\ 0 & T < T_m + \Delta T \end{cases} \tag{18}$$

where T_m is the solid–liquid phase transition temperature of the silicon material (K), and ΔT is the size of the 1/2 temperature range of the phase transition "mushy zone" when the phase transition occurs.

Results and discussion

Verification of the model

The mushy zone and solid zone are regarded as a whole without flow to simplify the model. To verify the accuracy of the model, the transient temperature field at the surface of melt during the downward process was calculated. During the experiment, a non-contact infrared thermometer was used to record the temperature of the center of the melt surface every 10 min. For comparison, the temperature measurement experiment was conducted under the same condition. Figure 2 shows the measured and calculated temperature value, which indicates that the computed temperature agrees well with the experimental measurements. The error between the measured value and the calculated value is within 10%.

Effects of pulling-down rate on the separation of Si from Ti-89 wt% Si melt

In controlling the melt flow and optimizing the crystal growth process, the electromagnetic field has proven to be a promising way [22, 23]. In our case, the flow field distribution induced by the intermediate frequency electromagnetic field in the melt is presented in Fig. 3 by the velocity streamline and plot when the power is 4.6 kW, the pull-down rate is 10 μm s^{-1}, and the solidification fraction is 0.25, 0.5, and 0.75, respectively. It can be seen from the flow pattern on the left side of Fig. 3(a-1) that when the solidification fraction is 0.25, some of the melt near the crucible flows forwards up intensively along the sidewall, and shifts to clockwise gradually when it approaches the melt surface, then turns to the horizontal direction and flows toward the center. The
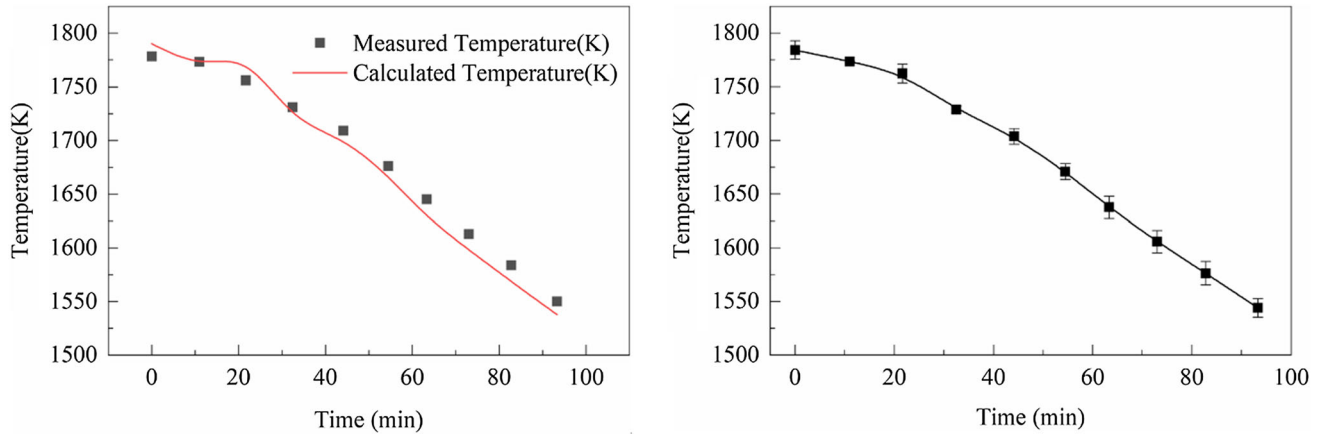
Figure 2 Measurement and calculation of temperature at 10 µm s^{-1} under an applied magnetic field.
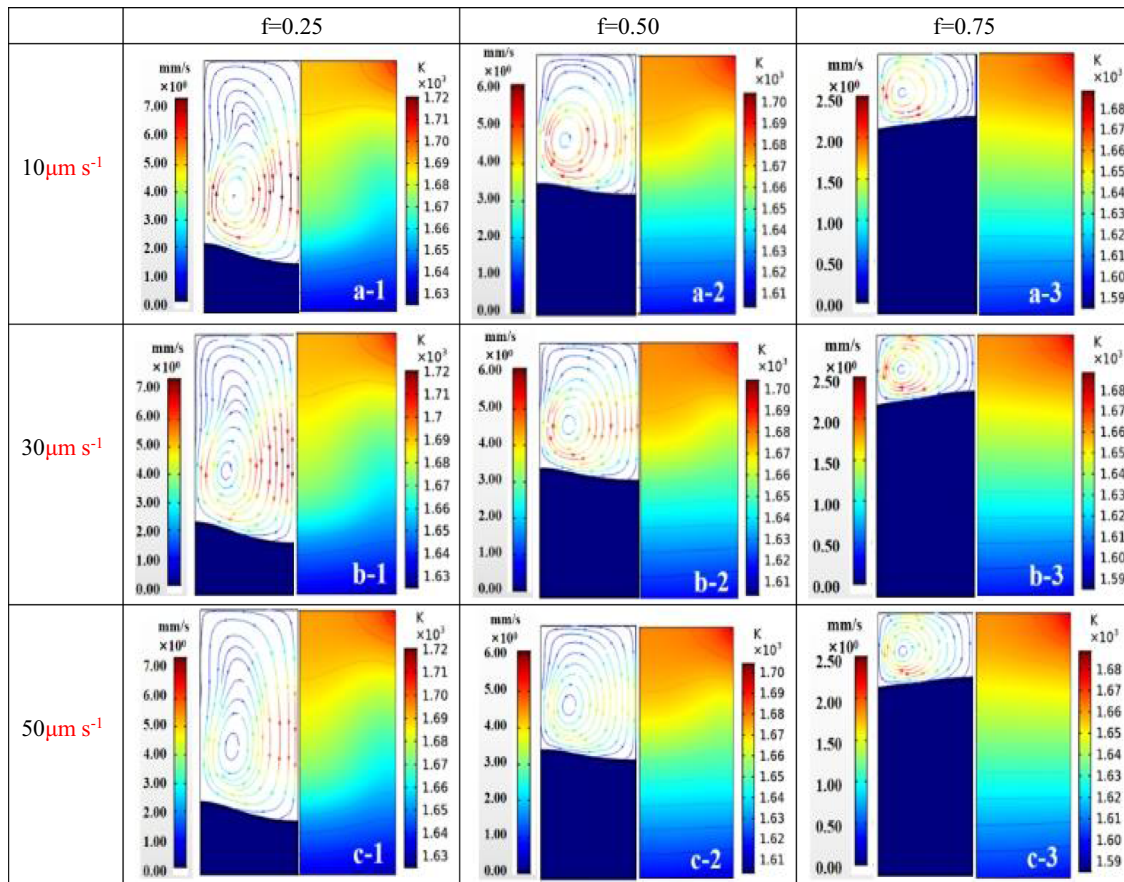
Figure 3 Flow field (Left) and heat field (Right) in the hypereutectic Ti-89 wt% Si melts during the electromagnetic directional solidification process with different pulling-down rate (*v*) and solidification fraction (*f*): **a-1** v = 10 µm s^{-1}, *f* = 0.25; **a-2** *v* = 10 µm s^{-1}, *f* = 0.5; **a-3** *v* = 10 µm s^{-1}, *f* = 0.75; **b-1** *v* = 30 µm s^{-1}, *f* = 0.25; **b-2** *v* = 30 µm s^{-1}, *f* = 0.5; **b-3** *v* = 30 µm s^{-1}, *f* = 0.75; **c-1** *v* = 50 µm s^{-1}, *f* = 0.25; **c-2** *v* = 50 µm s^{-1}, *f* = 0.5; **c-3** *v* = 50 µm s^{-1}, *f* = 0.75..

flow field converges at the center near the crucible wall and the (solid–liquid) S/L interface. The flow velocity near the melt center is higher than that in other regions. The flow pattern remains unchanged with the increase in solidification fraction, but the vortices shift slightly to the periphery of the melt, as

shown in Fig. 3(a-2, 3). According to the skin effect, it can be found that the closer to the edge of the crucible, the greater the electromagnetic force exerted on the melt, so that the melt edge has a larger flow velocity. Increasing the speed of the crucible away from the heating zone has an effect on the flow field of the melt, as shown in Fig. 3(b-1) and (c-1) under the condition of constant power. Obviously, the flow rate of melt near the crucible wall is decreasing.

Due to the skin effect, the heat source is not uniform in the melt. They are higher at the periphery (skin layer) of the melt and decrease in the center. Under this situation, the high-temperature melt will be brought from the periphery to the center of the melt and the solidification front by the eddies. As a result, the temperature distribution of the melt is more uniform, with the higher temperature concentrated in the center of the melt, which makes the isotherm concave. In the middle stage of solidification, the eddies which tend to the periphery are weakened, which leads to the decrease in temperature in the melt center and the isotherm is slightly concave. In the final stage, the temperature of the melt center is lower than that of the periphery due to the heat source gathering at the periphery and the further weakening of the eddy strength. Then, the isotherm changed from concave to convex.

For understanding the variation trend of velocity in the melt more intuitively, the velocity near the solid–liquid interface in the melt center is calculated, and the results are shown in Fig. 4a. The results show that the higher the solidification fraction, the lower the flow rate of the melt, when the drop-down speeds are constant. The higher pulling-down rate of the crucible of the same power and solidification fraction will result in a lower flow rate of the melt. Previous studies have found that the growth of silicon crystals is caused by the continuous migration of silicon atoms or clusters from the melt to the solidification front [24–26]. So, the migration mode in this study is mainly convection diffusion caused by melt flow,

$$k_c = \frac{u^2 r^2}{48D} \tag{19}$$

here, k_c is the convection diffusion coefficient, u is the fluid velocity, r is the characteristic length, and here is the crucible's inner diameter (mm). D is the molecular diffusion coefficient. According to the formula, the higher flow velocity is beneficial to the growth of silicon crystals.

Further, the relationship between the temperature gradient of melt near the S/L interface and the increase in the thickness of the solidified layer was investigated, and the results are shown in Fig. 4b. The temperature gradient curves indicate that under a certain condition of pulling rates and power, the temperature gradient in the melt is negatively related to the thickness of the ingot. Besides, with the increase in pulling speed, the temperature gradient at the front of the solid–liquid interface increases slightly, and the difference is in the range of 5 K mm^{-1}. Based on constant heat supply, the
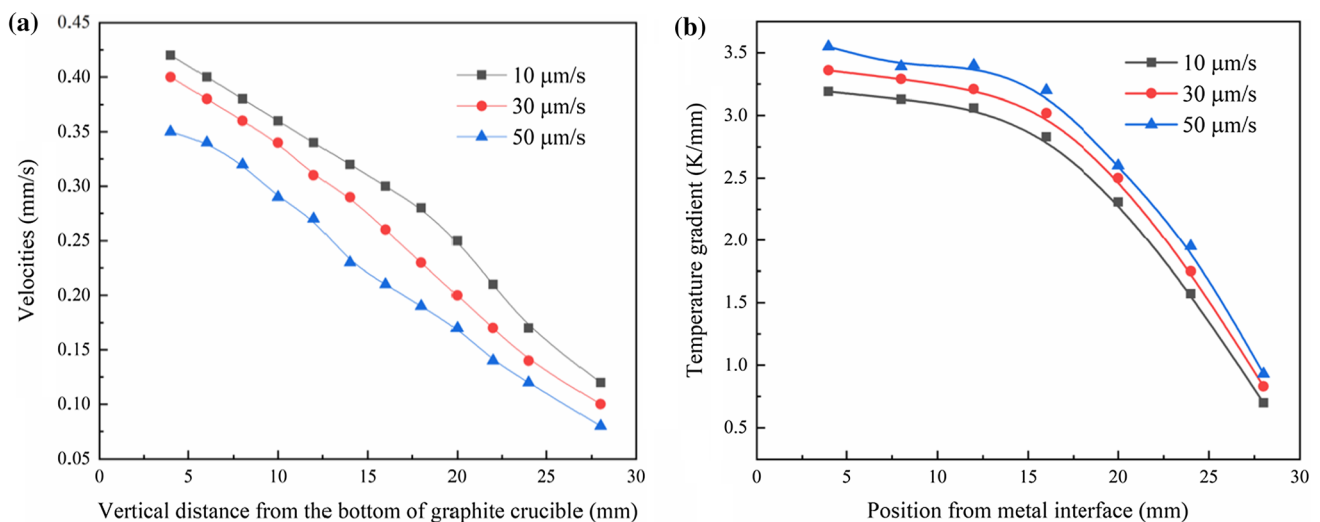
Figure 4 Numerical thermal parameters of the Ti-89 wt% Si alloy at different pulling-down rates under coil power of 4.6 kW: **a** velocity and **b** temperature gradient.

relationship between the cooling rate, pull-down rate, and temperature gradient is as follows,

$$v_c = v_z \bullet \frac{\partial T}{\partial z} \qquad (20)$$

here, v_c is the cooling rate (K s^{-1}); v_z is the pull-down rate (μm s^{-1}). Evidently, the increase in pulling-down rate will make the cooling rate increase. When the cooling rate is high, the silicon atoms do not have enough time to migrate to the solidification front, resulting in a decrease in the number of atoms the melt provides for the solidification front. Therefore, the lower pull speed can promote the separation of silicon crystals.

The macrostructure of the longitudinal section at different pulling rates is shown in Fig. 5. When the directional solidification is completed, the two different materials are observed and the dash in the middle is the separation interface. The silicon enrichment layer is found at the bottom of the crucible, and the remaining part is Ti–Si eutectic alloy region.

After the process of sanding and polishing, the microstructures of samples were analyzed. The microstructure in the middle of the silicon-rich region of Ti-89 wt% Si alloy at different pulling-down rates is shown in Fig. 6. According to the previous research, we can know that the gray area of microstructure represents the Si phase, the materials mixed in the Si phase are TiSi$_2$ eutectic alloys [27].

In the middle of the silicon-rich region, as shown in Fig. 6, the amount of titanium–silicon phase embedded between solidified silicon crystals decreases, under a pull-down rate of 10 μm s^{-1}. During the process of directional solidification, the vortex always promotes the migration of atoms to the solidification front. When the flow rate of melt changes from high to low, it means that the driving force of atoms or clusters in the melt becomes weak, and the migration of solidified crystals cannot be realized quickly. Yoshikawa et al. [28] studied that silicon starts solidifying at a low position in the sample and the solidified silicon crystals are carried to the bottom by a downward flow while subsequently adhering to each other. In our case, the flow rate of melt decreases from the increase in pulling rate, as shown in Fig. 4a. Then, with the increase in the downward speed, the TiSi$_2$ crystals do not have enough time migration under the weak driving force. Moreover, due to the higher cooling rate, the advancing speed of the solidification front increases, increasing TiSi$_2$ inclusions in the silicon-rich layer.

When the pulling rate is 10 μm s^{-1}, the average flow velocity of the melt is the largest during the entire electromagnetic directional solidification process, and the cooling rate of the melt is the smallest under the same solid fraction (s), which is conducive to the absorption of silicon atoms at the solidification front. When the pulling-down rate is μm s^{-1}, the Si+TiSi$_2$ phase inclusions in the silicon-rich layer gradually increase, and the TiSi$_2$ phase crystals in the Ti–Si alloy-rich layer are refined. Through (X-ray fluorescence) XRF detection of silicon content in the silicon enrichment layer, it is found that the enrichment effect of silicon is weakened, and the content is reduced to 88.04%.

As shown in Fig. 7, it is a sample of Ti-89 wt% Si which is fused under the conditions of 4.6 kW current and directional solidification rate of 10 μm s^{-1}. In the (energy-dispersive spectroscopy) EDS analysis of the sample boundary and a, b, it can be clearly seen that the sample is in two phases gray and white, the

Figure 5 Longitudinal macrostructures of Ti-89 wt% Si alloy samples solidified at different pulling-down rates under coil power of 4.6 kW: **a** 10 μm s^{-1}; **b** 30 μm s^{-1}; and **c** 50 μm s^{-1}.
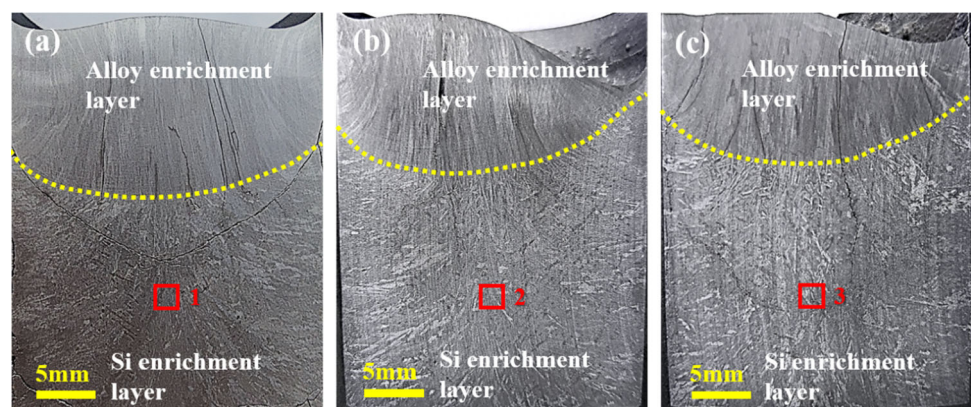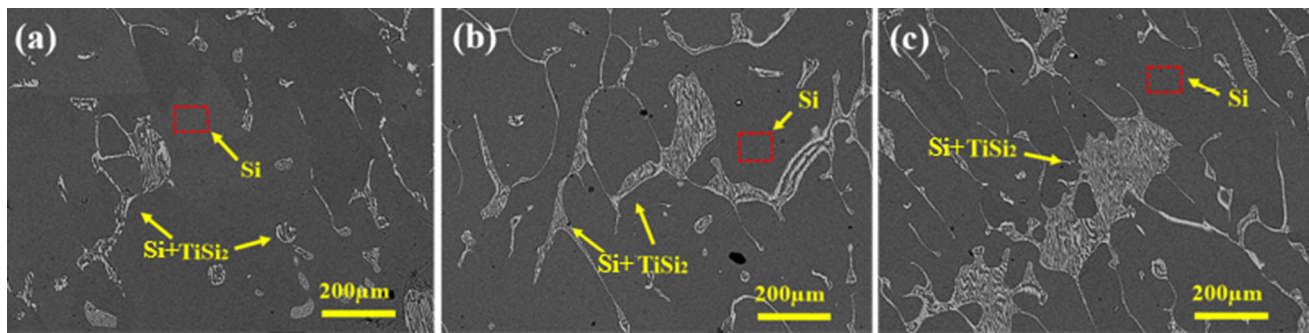
Figure 6 Silicon enrichment region of Ti-89 wt% Si alloy at different pulling-down rates (marked in Fig. 6): **a** position 1; **b** position 2; **c** position 3.

gray is the Si phase, the white is the TiSi$_2$ phase, and the upper end uses the Si phase as the matrix TiSi$_2$ as the matrix. Among the secondary phases, the lower Si phase and TiSi$_2$ phase are evenly distributed and dense. As can be seen from Fig. 7(a-1) to (a-3), it can be seen that the Si phase and the TiSi$_2$ phase are both elongated and dendritic intertwined, with uniform distribution and dense texture. As can be seen from Fig. 7(b-1) to (b-3), it can be seen that the TiSi$_2$ phase is wrapped in the Si matrix and presents a messy dendritic shape, with different sizes and poor distribution uniformity, without obvious impurity phases. In the process of directional solidification of titanium-silicon alloy, the segregation coefficient of Ti between the primary crystal silicon and the alloy melt is much less than 1. When the driving force of directional solidification is greater than the driving force of atoms or clusters, this will result in a large part of Ti migrating upwards, and after TiSi$_2$ nucleates and grows, it will be wrapped by silicon melt to maintain the bottom Ti at a certain concentration. The Ti content of the silicon-enriched layer is related to the speed of directional solidification. The higher the speed, the Ti content higher [29].

Effects of coil power on the separation of Si from Ti-89 wt% Si melt

Figure 8a–c shows that the melt flow field and heat field is affected by the parameter change of power when the pull-down rate is 10 μm/s, and the power is 3.8 kW, 4.6 kW, and 5.4 kW, respectively.

The melt flow pattern at different power is similar to those in Fig. 3. However, under the same pull-down rate, the increase in power has a positive effect on the enhancement of melt flow rate. Compared with Fig. 8(a-1), (b-1), and (c-1), the increase in power leads to a larger range of fierce melt flow. When the downward speed is constant, compared with the temperature field under a certain solidification fraction, it can be found that the upper limit of temperature in the melt increase from the increase in power, as shown in Fig. 8.

Similarly, the velocity and temperature gradient near the S/L interface in the melt center is calculated, as shown in Fig. 9. Under the condition of constant power, the velocity in the melt decreases from the increase in solidification fraction. When the solidification fraction is the same, the flow rate of the melt increases with the increase in power, which means that the driving force for the migration of silicon atoms in the melt is enhanced.

Due to the cooling conditions remain unchanged, the temperature gradient at 5.4 kW is higher than 3.8 kW, as shown in Fig. 9b. When the pull-down rate is 10 μm/s, as the power increases, the temperature gradient at the same position of different Si-rich layers increases. In the electromagnetic directional solidification process, as the temperature gradient increases, the natural convection formed by the melt under the action of gravity also increases, which is beneficial to the migration of silicon atoms.

The identical height region of the longitudinal section of various ingots was taken in the alloy enrichment layer for detection and analysis (marked positions 4, 5 and 6 in Fig. 10). The results are displayed in Fig. 11. As can be seen from the figure, as the power increases, the length of the strip-shaped TiSi$_2$ crystal becomes shorter. According to the numerical simulation results, as the power gradually increases, the current density in the melt increases, and the electromagnetic stirring effect is enhanced. When the power is large, the growth of grains in the

Figure 7 SEM analysis of sample Ti-89wt% Si; **a1**–**a3** SEM/EDS analysis of point a; **b1**–**b3** SEM/EDS analysis of point b.
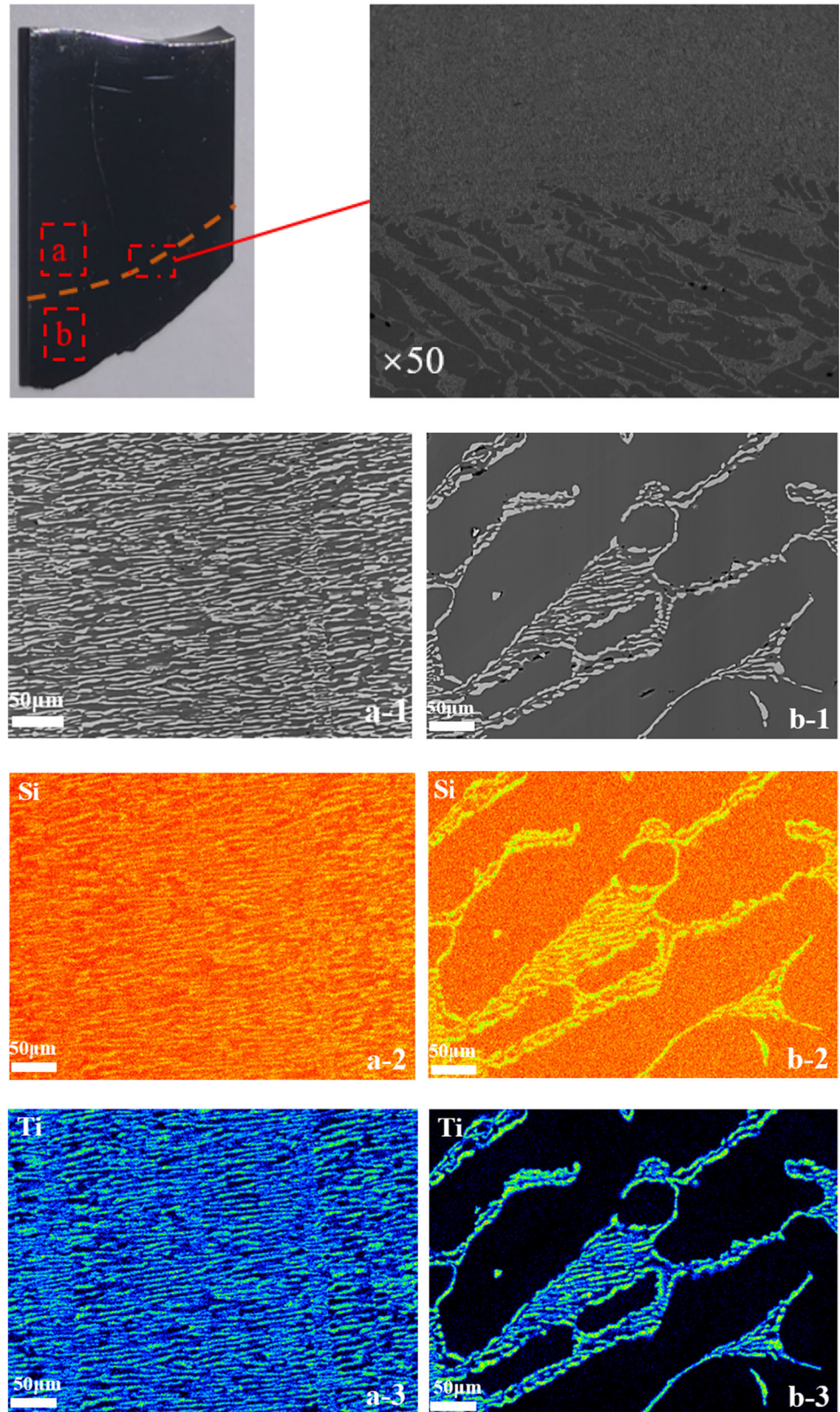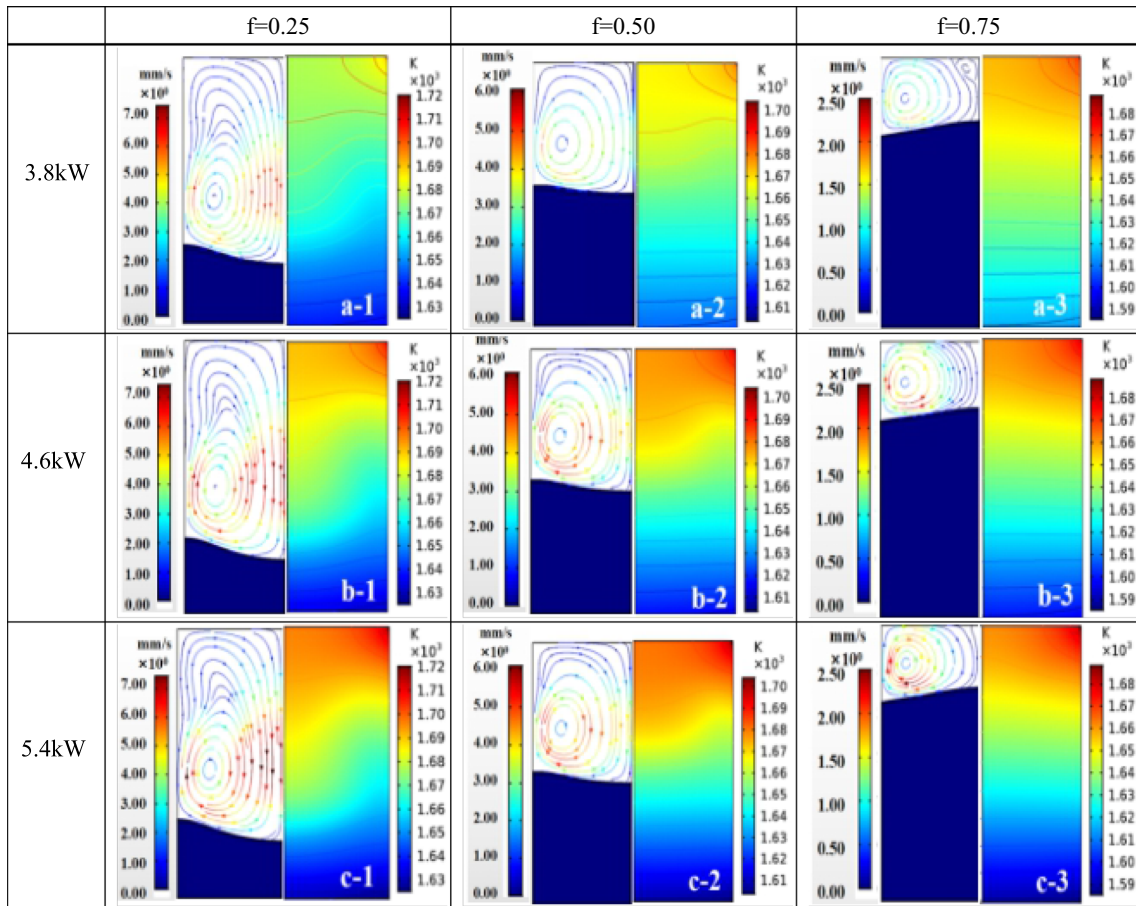
Figure 8 Flow field (Right) and heat field (Left) in the hypereutectic Ti-89 wt% Si melts during the electromagnetic directional solidification process with different coil power (*i*) and solidification fraction (*f*): **a-1** $i = 3.8$ kW, $f = 0.25$; **a-2** $i = 3.8$ kW, $f = 0.5$; **a-3** $i = 3.8$ kW, $f = 0.75$; **b-1** $i = 4.6$ kW, $f = 0.25$; **b-2** $i = 4.6$ kW, $f = 0.5$; **b-3** $i = 4.6$ kW, $f = 0.75$; **c-1** $i = 5.4$ kW, $f = 0.25$; **c-2** $i = 5.4$ kW, $f = 0.5$; **c-3** $i = 5.4$ kW, $f = 0.75$..
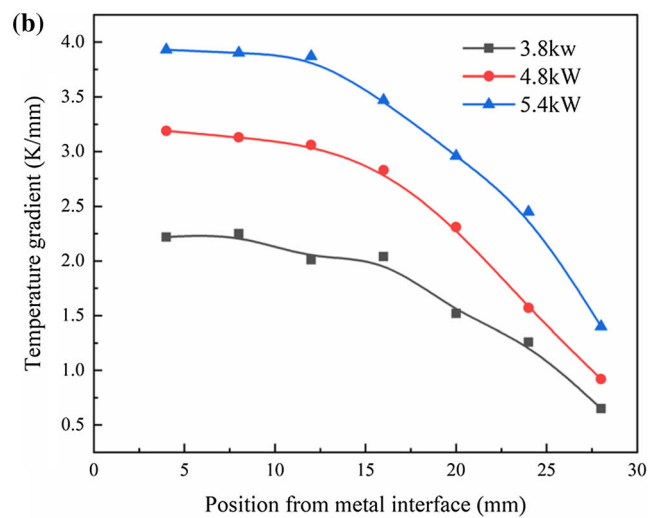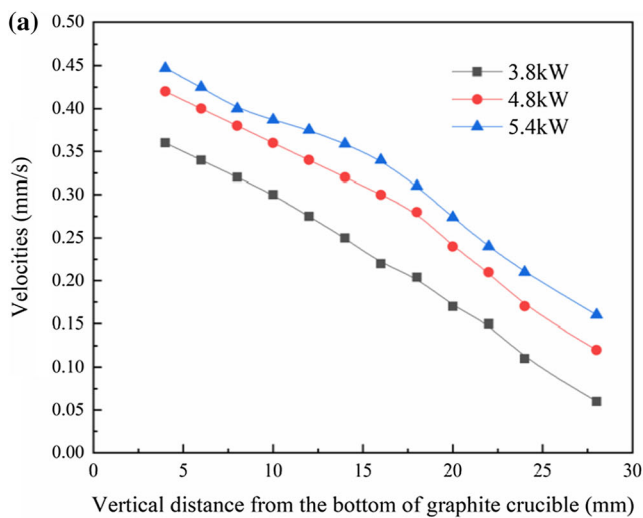
**Figure 9** Numerical thermal parameters of the Ti-89 wt% Si alloy at different coil power under the pulling-down rate of 10 μm s^{-1}: **a** velocity and **b** temperature gradient.

Figure 10 Longitudinal macrostructures of Ti-89 wt% Si alloy samples solidified at different coil power under the pulling-down rate of 10 μm s^{-1}: **a** 3.8 kW; **b** 4.6 kW; and **c** 5.4 kW.
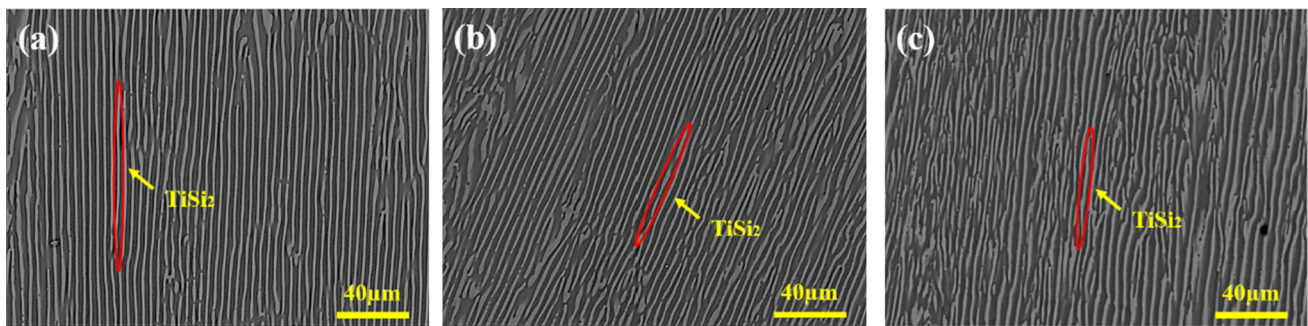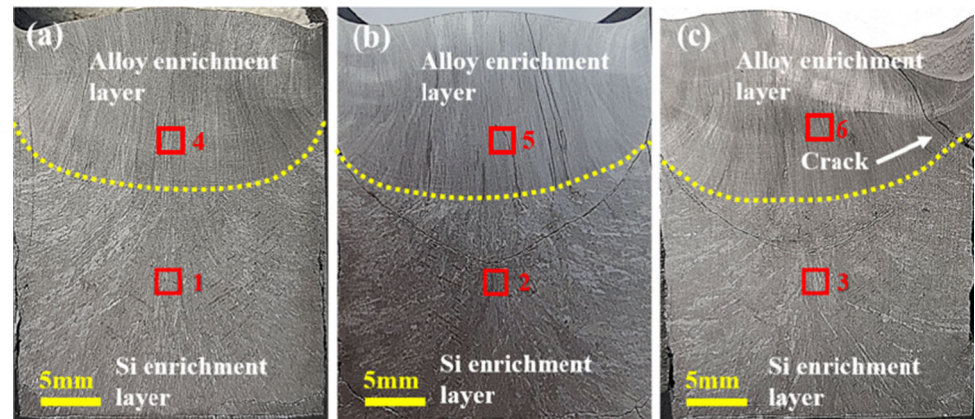
Figure 11 Microstructures at the same height at different power in Fig. 10: **a** position 4; **b** position 5; **c** position 6.
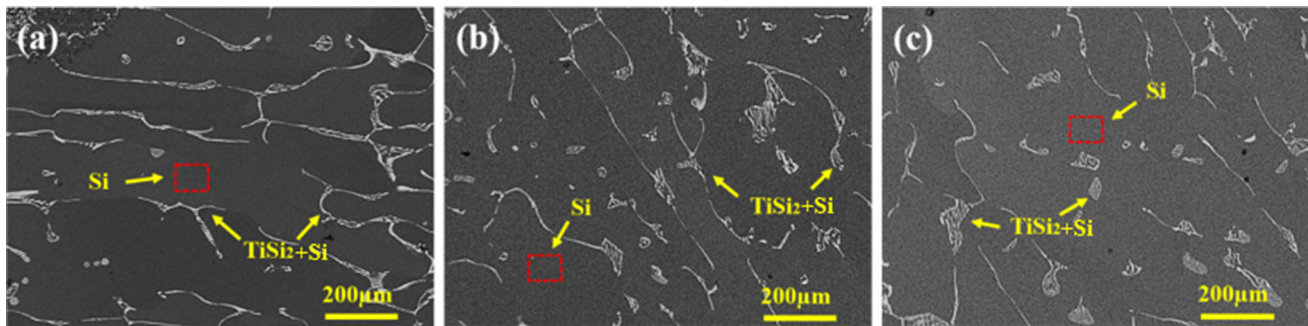

Figure 12 Silicon enrichment region of Ti-89 wt% Si alloy at different coil power (marked in Fig. 10): **a** position 1; **b** position 2; **c** position 3.

melt will be inhibited due to strong convection, and the crystal tip will be easily broken.

Therefore, as shown in Fig. 12, the number of inclusions that were engulfed during the movement of the solidification front decreased. In addition, the experimentally obtained Ti content in the enrich layer by ICP decreased from 4.16 to 2.08% with the increase in the power from 3.8 to 5.4 kW, as shown in Fig. 13.

Conclusions

For Ti-89% wt. Si alloy in electromagnetic directional solidification, the flow field and heat field were numerically investigated, and the macro/microstructure under magnetic field was studied. The results and conclusions can be summarized as follows:
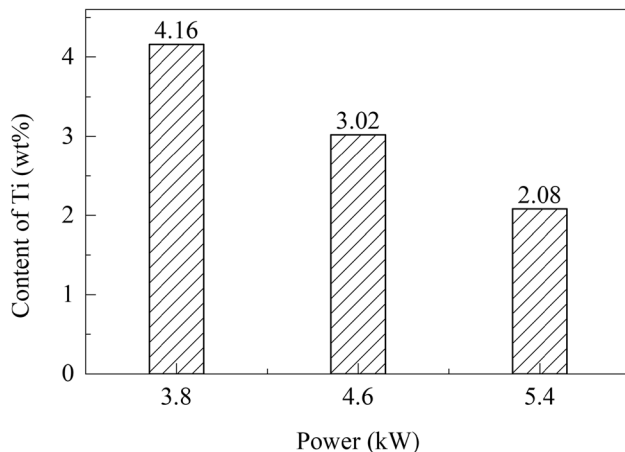
Figure 13 The Ti content of Si-rich area of samples dealt with different coil power.

1. With the directional solidification rate increases from 10 to 50 $\mu m\ s^{-1}$, the melt flow rate gradually decreases. Combined with the experiment, it can be seen that when the directional solidification rate is 50 $\mu m\ s^{-1}$, the content of Ti in the silicon enrichment layer increases.
2. When the electromagnetic directional solidification rate is constant, the increase in power increases the electromagnetic stirring effect and temperature gradient of the melt, which is beneficial to the migration of silicon atoms and has a positive effect on the separation of silicon crystals.
3. When the power is 5.4 kW, the melt flow rate is the largest, and the silicon in the melt is enriched in the lower part of the crucible. By ICP analysis shows that the content of Ti in Si-rich layer is only 2.08%.

Acknowledgements

Declarations

Conflict of interest The authors declare that they have no conflict of interest.

References

[1] Li C, Liang B, Guo LH, Wu ZB (2006) Effect of mechanical activation on the dissolution of Panzhihua ilmenite. Miner Eng 19:1430–1438. https://doi.org/10.1016/j.mineng.2006.02.005

[2] Zhen YL, Zhang GH, Chou KC (2016) Carbothermic reduction of titanium-bearing blast furnace slag. High Temp Mater Process 35:309–319. https://doi.org/10.1515/htmp-2014-0159

[3] Zhen YL, Zhang GH, Chou KC (2016) Mechanism and kinetics of the carbothermic reduction of titanium-bearing blast furnace slag. Metal Res Technol 113:507–516. https://doi.org/10.1051/metal/2016039

[4] Zhang L, Zhang LN, Wang MY, Li GQ, Sui ZT (2006) Dynamic oxidation of the Ti-bearing blast furnace slag. ISIJ Int 46:458–465. https://doi.org/10.2355/isijinternational.46.458

[5] Wang MY, Zhang LN, Zhang L, Sui ZT, Tu GF (2006) Selective enrichment of TiO_2 and precipitation behavior of perovskite phase in titania bearing slag. Nonferrous Met Soc China Trans 16:421–425. https://doi.org/10.1016/S1003-6326(06)60072-1

[6] Ren QD, Hao SJ, Jiang WF, Zhang YZ, Zhang WP (2014) Study of comprehensive utilization on Ti-bearing blast furnace Slag. Appl Mech Mater 488:141–144. https://doi.org/10.4028/www.scientific.net/AMM.488-489.141

[7] Liu XH, Sui ZT (2002) Leaching of Ti-bearing blast furnace slag by pressuring. Trans Nonferrous Met Soc China 12:1281–1284. https://doi.org/10.19476/j.ysxb.1004.0609.2002.06.038

[8] Tong QJ, Qi T, Liu YM, Wang LN, Zhang Y (2007) Preparation of potassium titanate whiskers and titanium dioxide from titaniferrous slag using KOH sub-molten salt method. Chin J Process Eng 7:85–89. https://doi.org/10.3321/j.issn:1009-606X.2007.01.018

[9] Zhu KS, Ma WH, Wei KX, Lei Y, Hu JF, Lv TL, Dai YN (2018) Separation mechanism of $TiSi_2$ crystals from a Ti–Si eutectic alloy via directional solidification. J Alloys Compd 750:102–110. https://doi.org/10.1016/j.jallcom.2018.02.161

[10] Zhu KS, Hu JF, Ma WH, Wei KX, Lv TL, Dai YN (2019) Effects of solidification parameters and magnetic field on separation of primary silicon from hypereutectic Ti-85 wt% Si melt. J Cryst Growth 522:78–85. https://doi.org/10.1016/j.jcrysgro.2019.05.012

[11] Yu QH, Liu LJ, Li ZY, Shao Y (2018) Parameter study of traveling magnetic field for control of melt convection in directional solidification of crystalline silicon ingots. Int J Heat Fluid Flow 71:55–67. https://doi.org/10.1016/j.ijheatfluidflow.2018.03.007

[12] Yang JR, Chen RR, Ding HS, Su YQ, Huang F, Guo JJ, Fu HZ (2012) Numerical calculation of flow field inside TiAl melt during rectangular cold crucible directional solidification. Trans Nonferrous Met Soc China 22:157–163. https://doi.org/10.1016/S1003-6326(11)61155-2

[13] Yang JR, Chen RR, Ding HS, Guo JJ, Su YQ, Fu HZ (2014) Flow field and its effect on microstructure in cold crucible directional solidification of Nb containing TiAl alloy. J Mater Process Technol 213:1355–1363. https://doi.org/10.1016/j.jmatprotec.2013.04.006

[14] Yang X, Ma WH, Lv GQ, Wei KX, Luo T, Chen DT (2014) A modified vacuum directional solidification system of multicrystalline silicon based on optimizing for heat transfer. J Cryst Growth 400:7–14. https://doi.org/10.1016/j.jcrysgro.2014.04.025

[15] Yu WZ, Ma WH, Lv GQ, Xue HY, Li SY, Dai YN (2014) Effect of electromagnetic stirring on the enrichment of primary silicon from Al–Si melt. J Cryst Growth 405:23–28. https://doi.org/10.1016/j.jcrysgro.2014.07.035

[16] Lv GQ, Bao Y, Zhang YF, He YF, Ma WH, Lei Y (2018) Effects of electromagnetic directional solidification conditions on the separation of primary silicon from Al–Si alloy with high Si content. Mater Sci Semicond Process 81:139–148. https://doi.org/10.1016/j.mssp.2018.03.006

[17] Liu YC, Roux B, Lan CW (2007) Effects of accelerated crucible rotation on segregation and interface morphology for vertical bridgman crystal growth: visualization and simulation. J Cryst Growth 304:236–243. https://doi.org/10.1016/j.jcrysgro.2007.01.046

[18] Bellmann MP, Meese EA (2011) Effect of steady crucible rotation on the segregation of impurities in vertical bridgman growth of multi-crystalline silicon. J Cryst Growth 333:1–6. https://doi.org/10.1016/j.jcrysgro.2011.08.004

[19] Yang X, Lv GQ, Ma WH, Xue HY, Chen DT (2016) The effect of radiative heat transfer characteristics on vacuum directional solidification process of multicrystalline silicon in the vertical bridgman system. Appl Therm Eng 93:731–741. https://doi.org/10.1016/j.applthermaleng.2015.10.073

[20] Duo WC, Yang X, He YF, Li QJ, Wei KX, Lv GQ, Ma WH (2020) Effect of marangoni convection on ingot quality during vacuum directional solidification of polycrystalline silicon. J Vac Sci Technol 41:515–523. https://doi.org/10.13922/j.cnki.cjvst.202011019

[21] Lv GQ, Yang Y, Liu C, Ma WH, Chen DT, Jiang PY (2015) Effects of heat exchange condition on growth interface and thermal stress of polysilicon in vacuum direction solidification process. Trans Mater Heat Treat 36:231–236. https://doi.org/10.13289/j.issn.1009-6264.20150505.001

[22] Abricka M, Gelfgat Y, Krumins J (2002) Influence of combined electromagnetic fields on the heat/mass transfer in the bridgman process. Energy Convers Manage 43:327–333. https://doi.org/10.1016/S0196-8904(01)00106-6

[23] Umbrashko A, Baake E, Nacke B, Jakovics A (2006) Modeling of the turbulent flow in induction furnaces. Met Mater Trans B 37:831–838. https://doi.org/10.1007/s11663-006-0065-0

[24] Morita K, Yoshikawa T (2011) Thermodynamic evaluation of new metallurgical refining processes for SOG–silicon production. Trans Nonferrous Met Soc China 21:685–690. https://doi.org/10.1016/S1003-6326(11)60766-8

[25] Li PT, Ren SQ, Jiang DC, Li JY, Zhang L, Tan Y (2016) Effect of alternating magnetic field on the removal of metal impurities in silicon ingot by directional solidification. J Cryst Growth 437:14–19. https://doi.org/10.1016/j.jcrysgro.2015.12.007

[26] Wang PP, Lu HM, Lai YS (2014) Control of silicon solidification and the impurities from an Al–Si melt. J Cryst Growth 390:96–100. https://doi.org/10.1016/j.jcrysgro.2013.12.024

[27] Zhu KS, Hu JF, Ma WH, Wei KX, Lv TL, Dai YN (2019) Effects of solidification parameters and magnetic field on separation of primary Si from hypereutectic Ti-85 wt% Si melt. J Cryst Growth 522:78–95. https://doi.org/10.1016/j.jcrysgro.2019.05.012

[28] Yoshikawa T, Morita K (2008) Refining of silicon during its solidification from a Si–Al melt. J Cryst Growth 311:776–779. https://doi.org/10.1016/j.jcrysgro.2008.09.095

[29] Hu JF (2020) Fundamental research on removal of metal impurities during electromagnetic directional solidification of titanium–silicon alloy. MD Diss Kunming Univ Sci Technol